Dominant polar surfaces of colloidal II-VI wurtzite semiconductor nanocrystals enabled by cation exchange

Aixiang Wang[*†], *Wenjie Wang*[†], *Jiayi Chen*[‡], *Rundong Mao*[‡], *Yingping Pang*[‡], *Yunguo Li*[*§], *Wei Chen*[‡], *Dechao Chen*[‡], *Derek Hao*[⊥], *Bing-Jie Ni*[⊥], *Martin Saunders*[‖], *Guohua Jia*[*‡]

[†]School of Chemistry and Chemical Engineering, Linyi University, Linyi 276005, P.R. China.

[‡]Curtin Institute of Functional Molecules and Interfaces, Department of Chemistry, Curtin University, Bentley, WA 6102, Australia

[§]Department of Earth Sciences, Faculty of Mathematical and Physical Sciences, University College London, Gower Street, London WC1E 6BT, UK.

[⊥]Centre for Technology in Water and Wastewater (CTWW), School of Civil and Environmental Engineering, University of Technology Sydney (UTS), Ultimo, NSW 2007, Australia

[‖]Centre for Microscopy, Characterization and Analysis (CMCA), The University of Western Australia, Clawley, WA 6009, Australia

ABSTRACT: Polar surfaces of ionic crystals are of growing technological importance, with implications for the efficiency of photocatalysts, gas sensors and electronic devices. Creation of ionic nanocrystals with large percentages of polar surfaces is an option to improve their efficiency in aforementioned applications but is hard to be accomplished because they are less thermodynamically stable and prone to vanish during the growth process. Herein we developed a strategy that is capable of producing polar surface dominated II-VI semiconductor nanocrystals including ZnS and CdS, from copper sulfide hexagonal nanoplates through cation exchange reactions. The obtained hexagonal prism-shaped wurtzite ZnS hexagonal nanoplates have dominant {002} polar surfaces, occupying up to 97.8% of all surfaces. Density functional calculations reveal the polar surfaces can be stabilized by a charge transfer of 0.25 eV/formula from the anion-terminated surface to the cation-terminated surface, which also explains the presence of polar surfaces in the initial $Cu_{1.75}S$ hexagonal nanoplates with cation deficiency prior to cation exchange reactions. Experimental results showed that the HER activity could be boosted by the surface polarization of polar surface dominated ZnS hexagonal nanoplates. We anticipate this strategy is general and could be used to other systems to prepare nanocrystals with dominant polar surfaces. Furthermore, the availability of colloidal semiconductor nanocrystals with dominant polar surfaces produced through this strategy open a new avenue for improving their efficiency in catalysis, photocatalysis, gas sensing and other applications.

TOC GRAPHICS

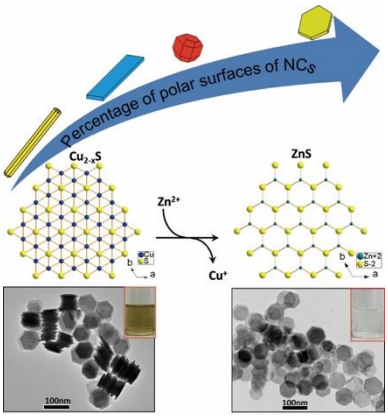

KEYWORDS: Polar surfaces, cation exchange, hexagonal nanoplates, density functional theory, ZnS

Despite the entire unit cell of an ionic crystal is neutral, the charge distribution may take specific configurations, resulting in positively charged and negatively charged surfaces which are called polar surfaces.[1–4] One of the most interesting consequences of this phenomenon is that certain polar surfaces of ionic crystals will create a macroscopic electrostatic field across the crystal.[5] The electric fields in the near-surface space charge regions influence the spatial charge distribution by promoting the charge separation and accumulating electrons and holes on the two end surfaces perpendicular to the electric field,[6–11] resulting in super photocatalytic activities and enhanced sensitivity, with relevance to a wide range of applications in catalysis, photocatalysis, gas sensing, piezoelectronics and magnetoresistive devices.[12–19]

Compared with non-polar surfaces, polar surfaces of nanocrystals usually have higher energy and therefore they are thermodynamically unstable. To minimize the energy of the systems, these polar surfaces tend to diminish and even vanish during the growth process, producing nanocrystals dominated by thermodynamically stable surfaces with low surface energy. Thus the production of nanocrystals with exposed polar high-energy surfaces is

important but challenging. To this end, tremendous efforts have been devoted in the development of controllable synthesis of nanocrystals with dominant high-energy surfaces and exploiting their enhanced surface properties for photocatalytic and sensing applications, as demonstrated in a variety of materials including ZnO,[5,12,14,15,17,18,20,21] TiO_2[13,22–24] and CeO_2.[25–27] Although some studies have been done in understanding the polarity and stability of the polar surfaces of CdSe[28-29] and PbSe[30] nanocrystals, to the best of our knowledge, however, traditional II-VI semiconductor nanocrystals (including zinc and cadmium chalcogenides but excluding ZnO) with dominant polar surfaces have yet been reported and the stabilization mechanisms were less understood.

We report on a facile approach for preparing II-VI semiconductor nanocrystals with dominant polar surfaces from copper sulfide nanocrystals through cation exchange reactions (see Materials and Methods in the Supporting Information for details). In comparison to colloidal semiconductor nanocrystals prepared by the wet-chemical approaches which only have very small percentages of polar surfaces, ZnS hexagonal nanoplates synthesized through cation exchange reactions were dominated by high-energy polar {002} surfaces, accounting for as high as 97.8% among all surfaces of the nanocrystals.

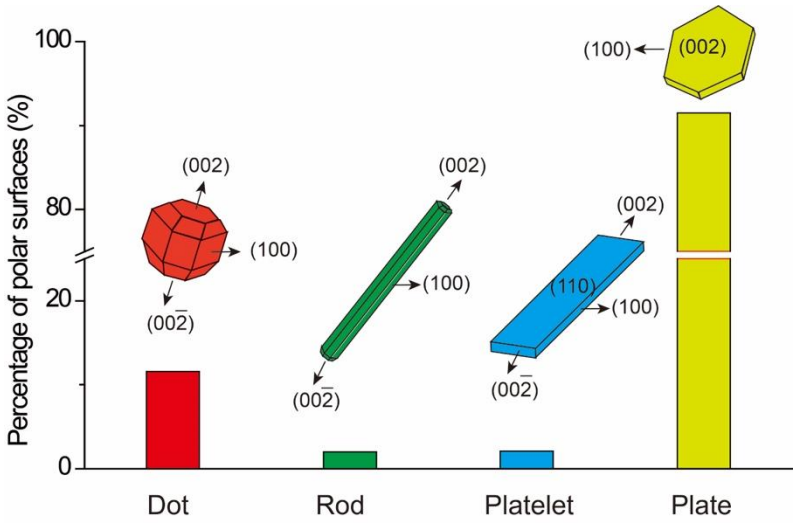

Scheme 1. Percentage of the {002} polar surfaces of wurtzite ZnS nanocrystals with various morphologies including dot, rod, rectangular platelet and hexagonal plate.

We herein use wurtzite ZnS as an illustrative example to substantiate how the percentage of polar surfaces of all surfaces can be modulated by altering the morphologies from dot, rod and rectangular platelet to hexagonal plate (Scheme 1). A ZnS dot with a diameter of 4 nm has a zinc-terminated (002) polar surface and a sulfur-terminated ($00\bar{1}$) polar surface, with percentages of {002} polar surfaces of being ~11.6% (see Section 2 in the Supporting Information for details). The equator of a special dot consists of six non-polar (100) type surfaces, which are connected with the non-polar surfaces by a combination of (101) and (103) surfaces and steps.[31] When the *c*-axis of the wurtzite dot is elongated, the morphology of the dot particle changes into rod (4 nm in diameter and 20 nm in length), with the non-polar {100} side surfaces being the dominant surfaces.[32–36] Then the percentage of polar surfaces reduces to 2.0% (see Section 2 in the Supporting Information for details). As for a rectangular nanoplatelet sample (with a width of 13 nm, length of 60 nm and thickness of 1.4 nm), the basal (110) surfaces are connected by the (100) surfaces, forming a rectangular prism with each end terminated with the {002} polar surfaces.[37,38] The percentage of polar surfaces of a plate sample is about 2.1%, which is very similar to that of a rod sample. When the {002} becomes the dominant surfaces, the sample turns into a hexagonal plate (Scheme 1, with a lateral size of 500 nm and thickness of 5 nm), with a percentage of the polar surfaces of 97.8% (see Section 2 in the Supporting Information for details). The above analysis clearly shows that wurtzite ZnS nanocrystals with dominant polar surfaces are attainable through tailoring their morphologies.

Next, we used wet-chemical approaches to synthesize wurtzite ZnS nanocrystals with a variety of morphologies (Experimental Section in the Supporting Information). Experimental results showed that the syntheses of wurtzite ZnS nanocrystals with a small portion of polar surfaces such as dots (Figure S1), nanorods (Figure S2) and rectangular nanoplatelets (Figure S3) were feasibly achieved. However, synthesis of wurtzite ZnS hexagonal nanoplates with dominant polar surfaces as depicted in Scheme 1 is difficult by direct colloidal synthetic approaches. Thus it is of great importance to develop a new strategy that is capable of producing such colloidal II-VI semiconductor nanocrystals with dominant polar surfaces.

Rather than using the direct synthesis wet-chemical approaches, we therefore developed a procedure that is capable of producing polar surface dominated ZnS hexagonal nanoplates by exchanging Cu^{+} with Zn^{2+} in copper sulfide nanocrystals, as schematically illustrated in Figure 1a. Highly uniform copper sulfide hexagonal nanoplates were synthesized using a thermal decomposition method from single-source precursors developed previously by our group.[39] The hexagonal prism-shaped copper sulfide hexagonal nanoplates were dominated by two basal planes, with a lateral size of 120 ± 5 nm. Some hexagonal nanoplates shown in the transmission electron microscopy (TEM) images were stacked together due to the weak interparticle interaction (Figure 1b). A close inspection on the copper sulfide hexagonal nanoplates standing on their edges reveals that the thickness of the hexagonal nanoplates is ~5 nm (Figure 1c).

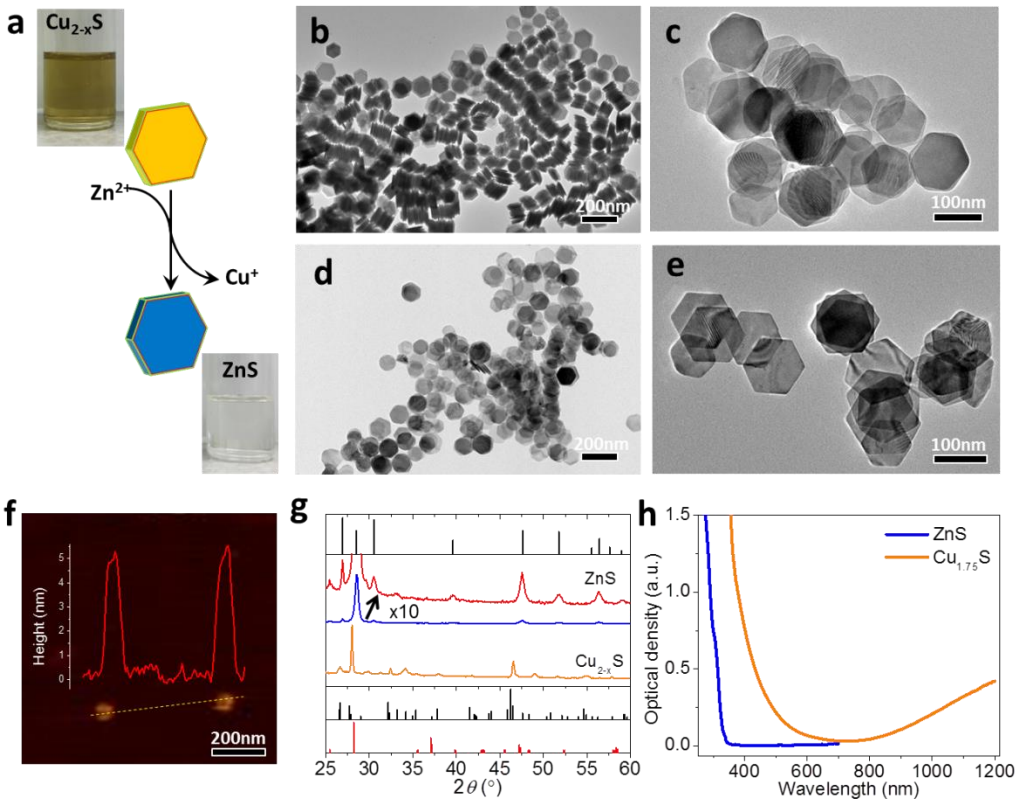

Figure 1. a) Schematic showing the production of ZnS hexagonal nanoplates from $Cu_{2-x}S$ hexagonal nanoplates through a cation exchange reaction. Photographs of both $Cu_{2-x}S$ and ZnS hexagonal nanoplates dispersed in toluene solutions were included showing the color change in relation to the cation exchange reactions. TEM images of b), c) $Cu_{2-x}S$ and d), e) ZnS hexagonal nanoplates. f) AFM image of ZnS hexagonal nanoplates and the associated height profile of individual ZnS hexagonal nanoplates marked by the yellow dashed line. g) Comparison of XRD patterns of ZnS (blue pattern) and $Cu_{2-x}S$ (orange pattern) hexagonal nanoplates. Inset shows an intensity scale expansion by 10 times (red pattern). The standard XRD cards for wurtzite ZnS (PDF#89-2942, top), hexagonal Cu_2S (PDF#26-1116, bottom) and anilite $Cu_{1.75}S$ (PDF#33-0489, bottom) were included for references. h) Comparison of absorption spectra of ZnS and $Cu_{2-x}S$ hexagonal nanoplates.

After the cation exchange reaction, the products retained both size and morphology of those of the initial copper sulfide hexagonal nanoplates (Figure 1d, 1e). The height profile of ZnS hexagonal nanoplates revealed by an atomic force microscopy (AFM) image confirmed that the thickness of the produced ZnS hexagonal nanoplates is ~5 nm, suggesting the thickness of the nanocrystals also maintained as that of the initial copper sulfide hexagonal nanoplates. X-ray

diffraction (XRD) pattern of the initial and final samples were compared in Figure 1g. As seen from the XRD pattern (Figure 1g), the diffraction peak at 28.1° can be indexed to the hexagonal Cu_2S phase (high-chalcocite) with a space group of *P63/mmc* and the rest of the satellite peaks match anilite $Cu_{1.75}S$ phase, with the diffraction intensity of diffraction peak at 28.1° being one magnitude stronger than those of other peaks. This suggests that the product of copper sulfide hexagonal nanoplates contains a predominant hexagonal Cu_2S phase together with an anilite $Cu_{1.75}S$ phase. Upon cation exchange reaction, an evolution from mixed phases of hexagonal Cu_2S and anilite $Cu_{1.75}S$ of the initial sample (denoted as $Cu_{2-x}S$) (Figure 1g, bottom pattern in orange) to a phase that could be indexed into wurtzite ZnS (PDF#89-2942) for the fully exchanged sample (Figure 1g, middle pattern in blue) was observed, without the presence of any addition phases. Notably, the diffraction band centered at 28.5° corresponding to the (002) plane of wurtzite ZnS hexagonal nanoplates is much broader than others in the XRD pattern (Figure 1g). The remarkably broaden feature of the diffraction corresponding to the (002) plane suggests that the obtained wurtzite ZnS hexagonal nanoplates have the smallest dimension along the [002] direction while the massive intensity of this diffraction peak indicates a large number of repetition of the crystal lattice along the (002) plane, being in consistence with morphology of ZnS nanocrystals revealed by TEM measurements in Figure 1d and 1e. Remarkably, the percentage of polar {002} surfaces out of all surfaces of the obtained ZnS hexagonal nanoplates is 83.9%, demonstrating that wurtzite ZnS hexagonal nanoplates with dominant polar {002} surfaces had been successfully produced through cation exchange reactions. Worthy of note is that, we were able to increase the percentage of {002} polar surfaces to ~97.8% in wurtzite ZnS hexagonal nanoplates, which were prepared from ultralarge lateral sized $Cu_{2-x}S$ hexagonal nanoplates[40] using the same cation exchange reactions (Figure S4).

Optical absorption spectroscopy provides further insights into the formation of ZnS hexagonal nanoplates from $Cu_{2-x}S$ hexagonal nanoplates through cation exchange reactions. As shown in Figure 1h, the absorption spectrum of the initial copper sulfide characterized by a localized surface plasmon resonance peak in the near-infrared range (orange curve in Figure 1h), which is consistent with the literature results.[41–43] The ZnS hexagonal nanoplates show an absorption edge with its maximum at 310 nm from which a band gap of 4.0 eV was extracted. This value is slightly larger than the band gap of the bulk wurtzite ZnS (317 nm, 3.91 eV)[44] due to the quantum confinement of carriers in ZnS hexagonal nanoplates. These results are consistent with the color change of solutions from brownish ($Cu_{2-x}S$) to colorless (ZnS) depicted in the photographs in Figure 1a.

To elucidate how hexagonal Cu_2S nanoplates evolve into hexagonal ZnS nanoplates, we firstly conducted partial cation exchange that produced Cu_2S-ZnS hexagonal hetero-nanoplates by adding insufficient amount of zinc precursors in the cation exchange reactions (See Supporting Information for details). As depicted in Figure 2a, the produced nanoparticle indeed showed two domains. High-resolution TEM (Figure 2b) and the associated fast Fourier transform (FFT) analysis confirmed that these two domains were correlated to ZnS (Figure 2c) and Cu_2S (Figure 2d). The formation of Cu_2S-ZnS hexagonal hetero-nanoplates was further confirmed by high-angle annular dark-field imaging (HAADF)-scanning TEM (STEM) (Figure 2e) and STEM-energy dispersive X-ray (EDX) element mapping measurements (Figure 2f-j). Evidently, the Cu_2S domain in the HAADF-STEM image (Figure 2e) had a better contrast compared with ZnS one, which is consistent with the larger mass of Cu_2S. The STEM-EDX element maps (Figure 2f-j) indeed corroborate the formation of Cu_2S-ZnS hexagonal hetero-nanoplates with homogenous distribution of all the copper, zinc and sulphur elements.

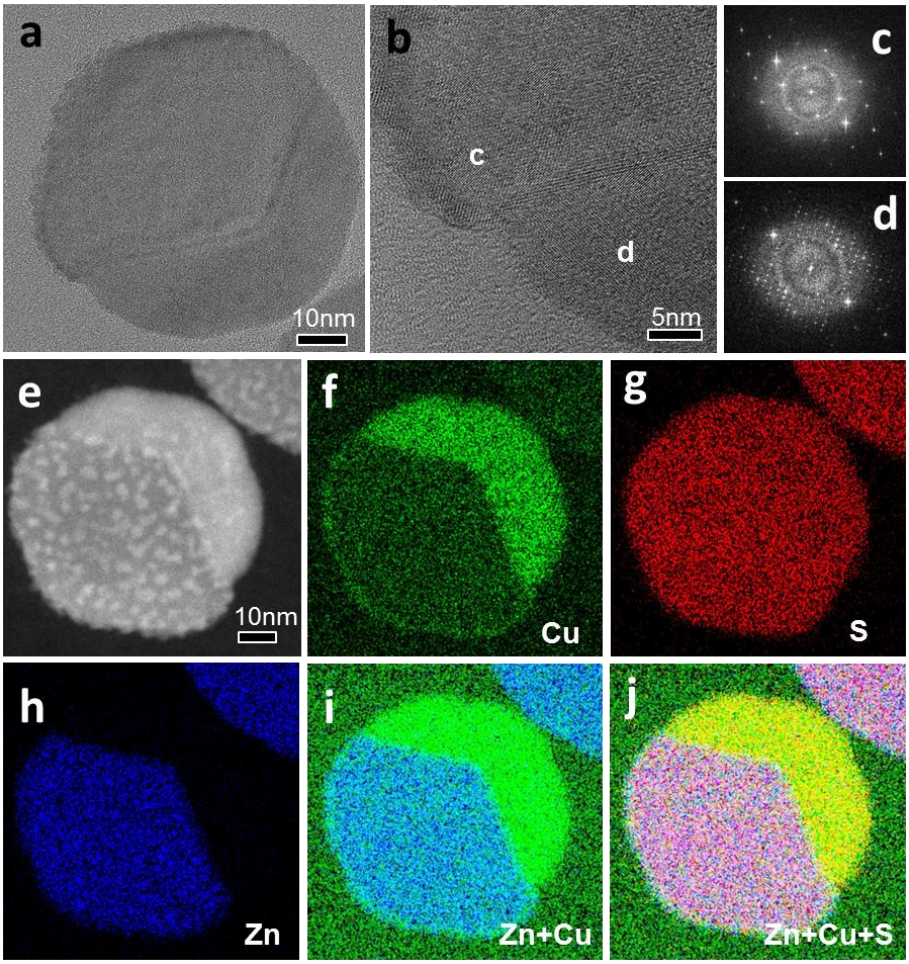

Figure 2. a) TEM b) HRTEM images of Cu_2S-ZnS hexagonal hetero-nanoplates produced by partial cation exchange. c) and d) are FFTs of the marked areas in b). e) HAADF-STEM image and f-j) element maps of Cu_2S-ZnS hexagonal hetero-nanoplates.

A TEM image of a typical ZnS hexagonal nanoplate with ultralarge lateral size is presented in Figure 3a. Some wrinkles were observed on the ultralarge sized ZnS hexagonal nanoplates, which could be induced by the relaxation of the crystal lattices in two-dimensional thin nanostructures (Figure S5).[39] HRTEM analysis on the selected area marked by a red rectangle of an individual ZnS hexagonal nanoplate in Figure 3a showed that the spacing of the lattice planes is 0.33 nm, corresponding to a typical distance of the {100} planes (Figure 3b). Analysis of the crystal lattices (Figure 3b) showed that ZnS hexagonal nanoplates grew mainly along the six

symmetric directions of ±[100], ±[1-10] and ±[010], with zinc-terminated (002) polar surface and sulfur-terminated ($00\bar{2}$) polar surface as top and bottom basal planes, respectively. HRTEM analysis revealed that the cation exchange resulted in the formation of monocrystalline ZnS nanocrystals displaying the expected wurtzite structure, with no detectable defects, as shown in Figure 3c. The fast Fourier transform (FFT) analysis corresponding to Figure 3c showed a characteristic six-fold diffraction symmetry (Figure 3d) and matched well with the simulated one using Crystal Maker (Figure 3e), further confirming that the *c*-axis of the wurtzite structure is perpendicular to the basal planes of the ZnS hexagonal nanoplates.

Figure 3f compares the atomic sketches of the representing (101) lattice slabs of hexagonal Cu_2S (left panel) and the (100) lattice slabs of wurtzite ZnS. The similarity of the S frameworks of two phases is indeed noteworthy. The anion lattice of ZnS also maintains the same to ZnS. After substitution of Cu^+ ions by Zn^{2+} ions, the initial Cu_2S lattice underwent a contraction of 9.3% along the ab plane (a equals to 4.23 Å for Cu_2S and 3.84 Å for ZnS) and an expansion of 13.7% along the *c*-axis (c equals to 5.52 Å for Cu_2S and 6.28 Å for ZnS). Such a relatively small difference in the anion sublattice between two structures may explain why the S^{2-} anion sublattice remained unaltered during the cation exchange reactions.

We further conducted the electrochemical tests to elucidate the activity of polar surface dominated ZnS hexagonal nanoplates in catalytic hydrogen evolution reactions (HER) in comparison to that of regular ZnS nanocrystals (See the Supporting Information for details). Compared with regular ZnS rectangular nanoplatelets, polar surface dominated ZnS hexagonal nanoplates indeed showed enhanced HER performance (Figure S6). The onset overpotential of polar surface dominated ZnS hexagonal nanoplates and regular ZnS rectangular nanoplatelets is 183 mV and 263 mV, respectively. The results suggest that the HER activity can be boosted by

the surface polarization of polar surface dominated ZnS hexagonal nanoplates. Our experimental results demonstrated that polar surface dominated ZnS NCs indeed had enhanced activity in catalytic HER.

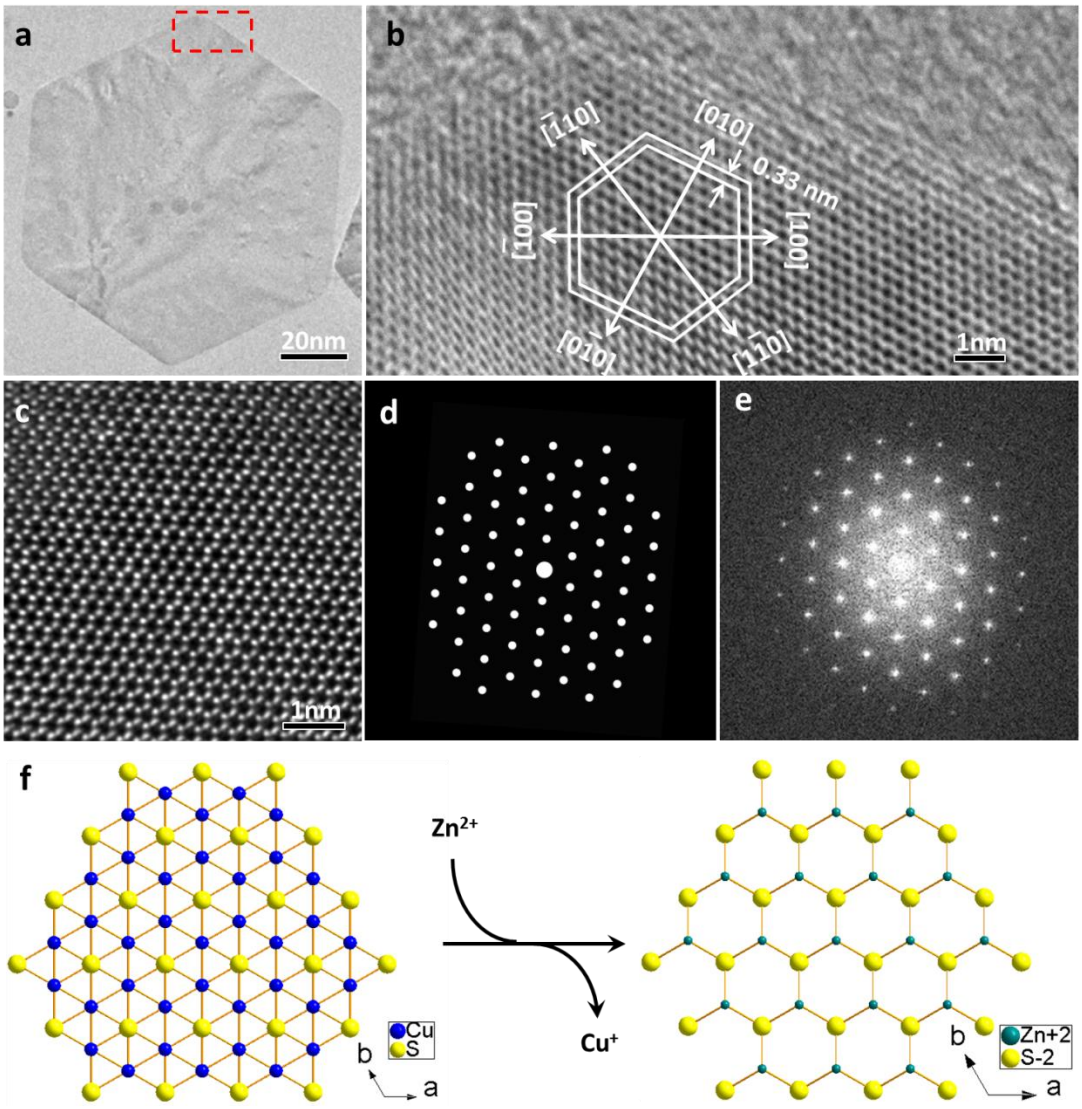

Figure 3. a) TEM image of ZnS hexagonal nanoplates. b) HRTEM image of the highlighted area in a). Inset shows the FFT of this image. c) HRTEM of a selected area of ZnS hexagonal nanoplates. d) Experimental and e) simulated FFTs of c). f) Atomic sketches of the representing (101) lattice slabs of hexagonal Cu_2S (left panel) and the (100) lattice slabs of wurtzite ZnS, showing the structural isomorphism of the two phases and the evident preservation of the anion sublattice during the cation exchange reaction.

To demonstrate the generality of this strategy, it has been used to synthesize hexagonal nanoplates with dominant polar surfaces of other II-VI semiconductors such as the benchmark material of CdS, starting from $Cu_{2-x}S$ hexagonal nanoplates. After the cation exchange reactions, the produced CdS nanocrystals preserved the size and morphology as those of the initial $Cu_{2-x}S$ hexagonal nanoplates (Figure 4a and 4b) and the XRD measurements showed that indeed the CdS structure was formed (Figure 4c). The diffraction band centered at 26.5° corresponding to the (002) plane of wurtzite CdS hexagonal nanoplates is much broader than others in the XRD pattern, which suggests the obtained CdS hexagonal nanoplates are dominated by the {002} polar surfaces (Figure 4c). For the cation exchange with Cd, the absorption onsets blue-shifted to ~450 nm, consistent with the smaller band gap of CdS and the yellowish color of the solution after cation exchange reactions (Inset Figure 4b). This demonstrates the expansion of the polar surface dominated hexagonal nanoplates through a straightforward reaction.

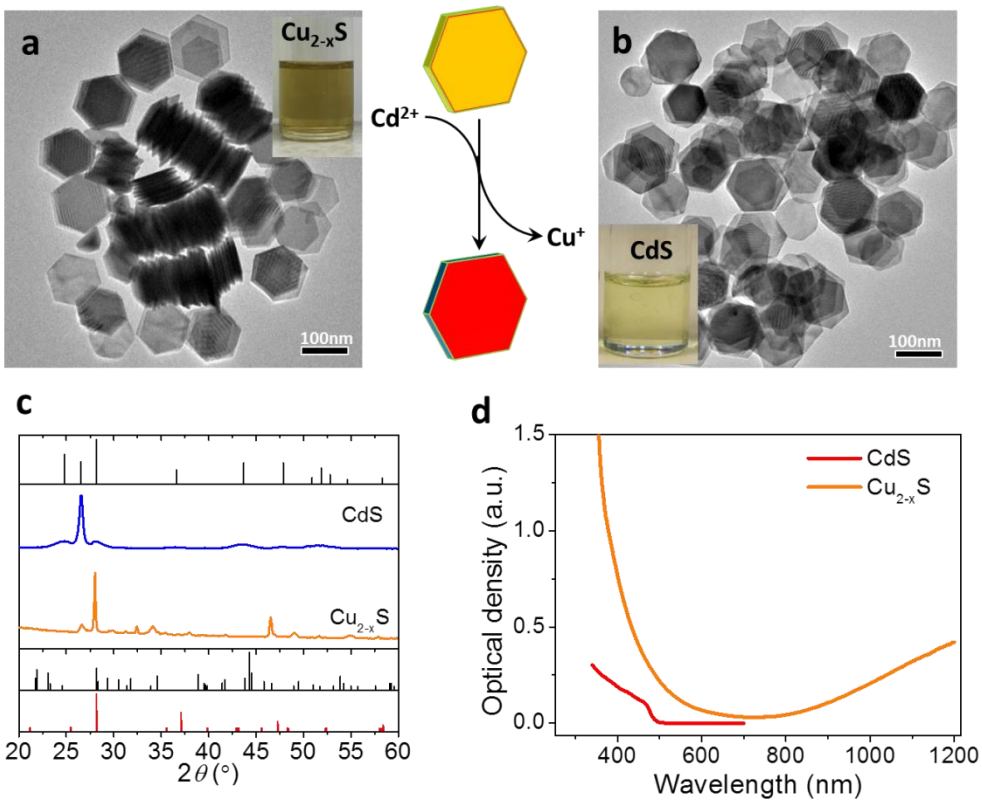

Figure 4. TEM images of the initial $Cu_{2-x}S$ hexagonal nanoplates and the produced CdS hexagonal nanoplates through cation exchange reactions. Inset photographs were toluene solutions dispersed with the hexagonal nanoplate samples. c) Comparison of XRD patterns of $Cu_{2-x}S$ and CdS hexagonal nanoplates. The standard XRD cards for wurtzite ZnS (PDF#89-2942, top), hexagonal Cu_2S (PDF#26-1116, bottom) and anilite $Cu_{1.75}S$ (PDF#33-0489, bottom) were included for references. d) Comparison of absorption spectra of $Cu_{2-x}S$ and CdS hexagonal nanoplates.

Clean-cut polar surfaces with a diverging electrostatic energy are unstable, but can be stabilized once the inherent dipole is counteracted by the processes like surface reconstruction. Previous studies on polar surfaces, especially the ZnO(001) and ZnO($00\bar{1}$) planes,[45–47] have been focusing on the surface structure and relaxation, while the essence of the stabilization mechanism has been neglected. No matter how the surface reconstructs and what pattern forms, the consequences are the reduction of net surface charge, and the surface is always composed of the dominant cation-terminated (anion- terminated) regions and anion-terminated (cation-terminated) patches, which, namely, acts as a charge transfer (or neutralizer).[48] In this study, we employed density functional theory (DFT) to gain further insights on the charge transfer mechanisms that are responsible for the stabilization of the dominant polar surfaces of colloidal semiconductor hexagonal nanoplates (see Materials and Methods in the Supporting Information for details).[49,50] To accomplish such an analysis, we need the surface energy of the polar surface (001) and ($00\bar{1}$) with different charge transfer between them. We therefore, developed a method to calculate this surface energy with variant charge transfer between the cation-terminated and anion-terminated surfaces (See Surface energy calculations in the Supporting Information for details). In practice, we built two slab supercells, one with the cation-terminated surfaces on both the top and bottom surfaces, and the other with the anion-terminated surfaces on both ends (Figure S7). There is a net charge on the surfaces, but no dipole in the slab. Then, we added electrons in the supercell with cation-terminated surfaces and remove the same number of electrons in the other with

anion-terminated surfaces, and the overall surface energy can be calculated. This surface energy corresponds to the average of the clean-cut polar surfaces (001) and $(00\bar{1})$ with different charge transfer from $(00\bar{1})$ to (001). In the meantime, the surface energy of individual (001) can be obtained given the cation chemical potential, and subsequently the surface energy of $(00\bar{1})$.

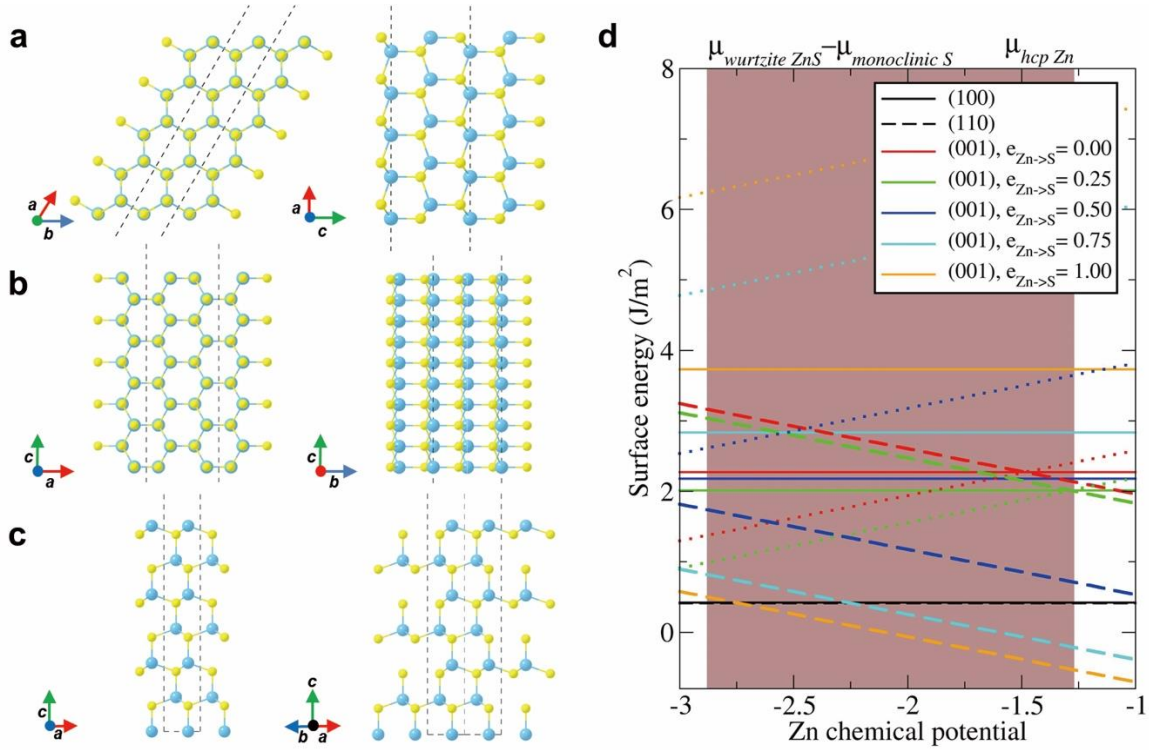

Figure 5. a) Stick-ball model of a) non-polar (100) surface, b) non-polar (110) surface, and c) polar (002) surfaces of wurtzite ZnS. Dashed lines indicate the boundary of supercell. d) Surface energy as a function of Zn chemical potential, which is bounded by the conditions: (1) μ(Zn) < μ_hcp (Zn); (2) μ(Zn)+μ_monoclinic (S)>μ_wurtzite (ZnS). For nonpolar surfaces (100) and (110), there is only one line for each. For (001) surface, it has three lines for each charge transfer, namely, the stochiometric surface in solid line, the Zn-terminated surface in dashed line and the S-terminated surface in dotted line.

Figure 5a-c compared the stick-ball model of (100), (110) non-polar surfaces and (002) polar surfaces of wurtzite ZnS, respectively. The calculated surface energy for (001) and $(00\bar{1})$

surfaces is shown in Figure 3d together with other (110) and (100) non-polar surfaces. The first important finding is that the average surface energy of (001) and $(00\bar{1})$ is at its lowest when the charge transfer is 0.25 electron per formula (Figure 5, Table S1). The amount of charge transfer needed to counterbalance the dipole should depend on the inherent bulk properties, however, it is exactly equal to the cation deficiency of Cu in $Cu_{1.75}S$. Besides, the (001) and $(00\bar{1})$ polar surfaces of ZnO were also found stabilized at a cation deficiency of ~0.24.[46] Whether it is a magic number is beyond the scope of this study and the ability of current method, but it couldn't be just a coincidence. The second finding is that the polar surface can be the most stable one under certain charge transfer and cation chemical potential. But to overtake nonpolar surfaces the charge transfer needs to be high (>0.5 electron per formula) for the polar surfaces. If charge transfer is realized via cation/anion vacancies on (001)/$(00\bar{1})$, this means a dramatic surface reconstruction; from another perspective, this is more like growing a cation/anion island on the anion-/cation-terminated surface.

In conclusion, we developed a strategy capable of producing polar surface dominated semiconductor nanocrystals, which is usually not accessible by the conventional wet-chemical approaches. Mechanistic studies revealed that the stabilization of the dominant polar surfaces of ZnS hexagonal nanoplates was achieved through a charge transfer of 0.25 eV/formula from the anion-terminated surface to the cation-terminated surface, which perfectly matches the experimental observations with $Cu_{1.75}S$ being the most stable phase. Polar surface dominated ZnS NCs indeed had enhanced activity in catalytic HER. This work sheds lights on the surface engineering of nanocrystals, with relevance to a wide range of photocatalytic and sensing applications.

ASSOCIATED CONTENT

Supporting Information.

The Supporting Information is available free of charge on the ACS Publications website at DOI: 10.1021/xxxx.

Nanocrystal synthesis, XRD, Absorption spectra, TEM images, and DFT calculations

AUTHOR INFORMATION

Corresponding Author

wangaixiang1974@163.com (A.W.)

yunguo.li@ucl.ac.uk (Y.L.)

guohua.jia@curtin.edu.au (G.J).

ACKNOWLEDGMENT

This work was supported by Australian Research Council (ARC) Discovery Early Career Researcher Award (DECRA) (Project ID: DE160100589), National Science Foundation of China (NSFC) (Project ID: 21675074 and 21777065). We thank Yingping Pang for assistance in synthesizing nanoparticles. The authors acknowledge the facilities, and the scientific and technical assistance of the Australian Microscopy & Microanalysis Research Facility at the Centre for Microscopy, Characterisation & Analysis, The University of Western Australia, a facility funded by the University, State and Commonwealth Governments.

REFERENCES

1. Kong, X. Y.; Ding, Y.; Yang, R.; Wang, Z. L. Single-Crystal Nanorings Formed by Epitaxial Self-Coiling of Polar Nanoelts. *Science* **2004**, *303*, 1348–1351.

2. Kong, L. B.; Li, T.; Hng, H. H.; Boey, F.; Zhang, T.; Li, S.; Waste Energy Harvesting: Mechanical and Thermal Energies. Springer, 2014; pp. 136.

3. Liu, Y.; Rowell, N.; Willis, M.; Zhang, M.; Wang, S.; Fan, H.; Huang, W.; Chen, X.; Yu, K. Photoluminescent Colloidal Nanohelices Self-Assembled from CdSe Magic-Size Clusters via Nanoplatelets. *J. Phys. Chem. Lett.* **2019**, 10, 2794–2801.

4. Boles, M. A.; Ling, D.; Hyeon, T.; Talapin, D. V.; The Surface Science of Nanocrystals. *Nat. Mater.* **2016**, *15*, 141–153.

5. Wander, A.; Schedin, F.; Steadman, P.; Norris, A.; McGrath, R.; Turner, T. S.; Thornton, G.; Harrison, N. M. Stability of Polar Oxide Surfaces. *Phys. Rev. Lett.* **2001**, *86*, 3811–3814.

6. Li, L.; Salvador, P. A.; Rohrer, G. S. Photocatalysts with Internal Electric Fields. *Nanoscale* **2014**, *6*, 24–42.

7. Bai, S.; Wang, L.; Li, Z.; Xiong, Y. Facet-Engineered Surface and Interface Design of Photocatalytic Materials. *Adv. Sci.* **2017**, *4*, 1600216.

8. Wang, S.; Liu, G.; Wang, L.; Crystal Facet Engineering of Photoelectrodes for Photoelectrochemical Water Splitting. *Chem. Rev.* **2019**, *119*, 5192–5247.

9. Wang, S.; Yu, J.; Zhang, M.; Chen, D.; Li, C.; Chen, R.; Jia, G.; Rogach, A. L.; Yang, X. Stable, Strongly Emitting Cesium Lead Bromide Perovskite Nanorods with High Optical Gain Enabled by an Intermediate Monomer Reservoir Synthetic Strategy. *Nano Lett.* **2019**, *19*, 6315–6322.

10. G, S.; Mahale, P.; Kore, B. P.; Mukherjee, S.; Pavan, M. S.; De, C.; Ghara, S.; Sundaresan, A.; Pandey, A.; Guru Row, T. N.; Sarma, D. D. Is $CH_3NH_3PbI_3$ Polar? *J. Phys. Chem. Lett.* **2016**, *7*, 13, 2412-2419.

11. Strong, S. E.; Eaves, J. D. Tetracene Aggregation on Polar and Nonpolar Surfaces: Implications for Singlet Fission, *J. Phys. Chem. Lett.* **2015**, *6*, 1209−1215.

12. Mclaren, A.; Valdes-Solis, T.; Li, G.; Tsang, S. C. Shape and Size Effects of ZnO Nanocrystals on Photocatalytic Activity. *J. Am. Chem. Soc.* **2009**, *131*, 12540–12541.

13. Zhang, A.-Y.; Wang, W.-Y.; Chen, J.-J.; Liu, C.; Li, Q.-X.; Zhang, X.; Li, W.-W.; Si, Y.; Yu, H.-Q. Epitaxial Facet Junction on TiO_2 Single Crystals for Efficient Photocatalytic Water sSplitting. *Energy Environ. Sci.* **2018**, *11*, 1444–1448.

14. Wang, X.; Yin, L.; Liu, G.; Wang, L.; Saito, R.; Lu, G. Q.; Cheng, H.-M. Polar Interface-Induced Improvement in High Photocatalytic Hydrogen Evolution over ZnO–CdS Heterostructures. *Energy Environ. Sci.* **2011**, *4*, 3976–3979.

15. Alenezi, M. R.; Alshammari, A. S.; Jayawardena, K. D. G. I.; Beliatis, M. J.; Henley, S. J.; Silva, S. R. P. Role of the Exposed Polar Facets in the Performance of Thermally and UV Activated ZnO Nanostructured Gas Sensors. *J. Phys. Chem. C* **2013**, *117*, 17850–17858.

16. Li, Z.; Zhang, L.; Liu, Y.; Shao, C.; Gao, Y.; Fan, F.; Wang, J.; Li, J.; Yan, J.; Li, R.; Li, C. Surface Polarity-Induced Spatial Charge Separation Boosting Photocatalytic Overall Water Splitting on GaN Nanorod Arrays. *Angew. Chem. Int. Ed.* **2020**, *59*, 935–942.

17. Chen, Y.; Zhao, H.; Liu, B.; Yang, H. Charge Separation Between Wurtzite ZnO Polar {001} Surfaces and Their Enhanced Photocatalytic Activity. *Appl. Catal. B-Environ.* **2015**, *163*, 189–197.

18. Wang, Z. L.; Kong, X. Y.; Ding, Y.; Gao, P.; Hughes, W. L.; Yang, R.; Zhang, Y. Semiconducting and Piezoelectric Oxide Nanostructures Induced by Polar Surfaces. *Adv. Funct. Mater.* **2004**, *14*, 943–956.

19. Soeya, S.; Nakamura, S.; Imagawa, T.; Narishige, S. Rotational Hysteresis Loss Study on Exchange Coupled $Ni_{81}Fe_{19}$/Nio Films. *J. Appl. Phys.* **1995**, *77*, 5838–5842.

20. Liu, X.; Afzaal, M.; Ramasamy, K.; O'Brien, P.; Akhtar, J. Synthesis of ZnO Hexagonal Single-Crystal Slices with Predominant (0001) and (000$\bar{1}$) Facets by Poly(ethylene glycol)-Assisted Chemical Bath Deposition. *J. Am. Chem. Soc.* **2009**, *131*, 15106–15107.

21. Iglesias-Juez, A.; Viñes, F.; Lamiel-García, O.; Fernández-García, M.; Illas, F. Morphology Effects in Photoactive ZnO Nanostructures: Photooxidative Activity of Polar Surfaces. *J. Mater. Chem.* **2015**, *3*, 8782–8789.

22. Zhang, A.-Y.; Long, L.-L.; Liu, C.; Li, W.-W.; Yu, H.-Q. Electrochemical Degradation Of Refractory Pollutants Using TiO_2 Single Crystals Exposed By High-Energy {001} Facets. *Water Res.* **2014**, *66*, 273–278.

23. Pei1, D.-N.; Gong, L.; Zhang, A.-Y.; Zhang, X.; Chen, J.-J.; Mu, Y.; Yu, H.-Q. Defective Titanium Dioxide Single Crystals Exposed By High-Energy {001} Facets for Efficient Oxygen Reduction. *Nat. Commun.* **2015**, *6*, 8696.

24. Pan, J.; Liu, G.; Lu, G. Q.; Cheng, H.-M. On the True Photoreactivity Order of {001}, {010}, and {101} Facets of Anatase TiO_2 Crystals. *Angew. Chem. Int. Ed.* **2011**, *50*, 2133–2137.

25. Capdevila-Cortada, M.; López, N. Entropic Contributions Enhance Polarity Compensation for CeO_2(100) Surfaces. *Nat. Mater.* **2017**, *16*, 328–334.

26. Kozlov, S. M.; Viñes, F.; Nilius, N.; Shaikhutdinov, S.; Neyman, K. M. Absolute Surface Step Energies: Accurate Theoretical Methods Applied to Ceria Nanoislands. *J. Phys. Chem. Lett.* **2012**, *3*, 15, 1956–1961.

27. Senanayake, S. D.; Sadowski, J. T.; Evans, J.; Kundu, S.; Agnol, S.; Yang, F.; Stacchiola, D.; Flege, J. I.; Hrbek, J.; Rodriguez, J. A. Nanopattering in CeOx/Cu(111): A New Type of Surface Reconstruction and Enhancement of Catalytic Activity. *J. Phys. Chem. Lett.* **2012**, *3*, 839–843.

28. Bertoni, G.; Grillo, V.; Brescia, R.; Ke, X.; Bals, S.; Catellani, A.; Li, H.; Manna, L. Direct Determination of Polarity, Faceting, and Core Location in Colloidal Core/Shell Wurtzite Semiconductor Nanocrystals. *ACS Nano* **2012**, *6*, 6453–6461.

29. Ghosh, S.; Gaspari, R.; Bertoni, G.; Spadaro, M. C.; Prato, M.; Turner, S.; Cavalli, A.; Manna, L.; Brescia, R. Pyramid-Shaped Wurtzite CdSe Nanocrystals with Inverted Polarity. *ACS Nano* **2015**, *9*, 8537–8546.

30. Fang, C.; van Huis, M. A.; Vanmaekelbergh, D.; Zandbergen, H. W. Energetics of Polar and Nonpolar Facets of PbSe Nanocrystals from Theory and Experiment. ACS Nano **2010**, *4*, 211–218.

31. Shiang, J. J.; Kadavanich, A. V.; Grubbs, R. K.; Alivisatos, A. P. Symmetry of Annealed Wurtzite CdSe Nanocrystals: Assignment to the C_{3v} Point Group. *J. Phys. Chem.* **1995**, *99*, 17417–17422.

32. Jia, G.; Banin, U. A General Strategy for Synthesizing Colloidal Semiconductor Zinc Chalcogenide Quantum Rods. *J. Am. Chem. Soc.* **2014**, *136,* 11121–11127.

33. Jia, G.; Sitt, A.; Hitin, G. B.; Hadar, I.; Bekenstein, Y.; Amit, Y.; Popov, I.; Banin, U. Couples of Colloidal Semiconductor Nanorods Formed by Self-Limited Assembly. *Nat. Mater.* **2014**, *13*, 301–307.

34. Chen, D.; Zhang, H.; Li, Y.; Pang, Y.; Yin, Z.; Sun, H.; Zhang, L.-C.; Wang, S.; Saunders, M. ; Barker, E.; Jia, G. Spontaneous Formation of Noble- and Heavy-Metal- Free Alloyed Semiconductor Quantum Rods for Efficient Photocatalysis. *Adv. Mater.* **2018**, *30*, 1803351.

35. Jia, G.; Pang, Y.; Ning, J.; Banin, U.; Ji, B. Heavy-Metal-Free Colloidal Semiconductor Nanorods: Recent Advances and Future Perspectives. *Adv. Mater.* **2019**, *31*, 1900781.

36. Shen, S.; Zhang, Y.; Peng, L.; Du, Y.; Wang, Q. Matchstick-Shaped Ag_2S–ZnS Heteronanostructures Preserving both UV/Blue and Near-Infrared Photoluminescence. *Angew. Chem. Int. Ed.* **2011**, *50*, 7115–7118.

37. Pang, Y.; Zhang, M.; Chen, D.; Chen, W.; Wang, F.; Anwar, S. J.; Saunders, M.; Rowles, M. R.; Liu, L.; Liu, S.; Sitt, A.; Li, C.; Jia, G. Why Do Colloidal Wurtzite Semiconductor Nanoplatelets Have an Atomically Uniform Thickness of Eight Monolayers? *J. Phys. Chem. Lett.* **2019**, *10*, 3465–3471.

38. Son, J. S.; Wen, X.-D.; Joo, J.; Chae, J.; Baek, S.-I.; Park, K.; Kim, J. H.; An, K.; Yu, J. H.; Kwon, S. G.; Choi, S.-H.; Wang, Z.; Kim, Y.-W.; Kuk, Y.; Hoffmann, R.; Hyeon, T. Large-Scale Soft Colloidal Template Synthesis of 1.4 nm Thick CdSe Nanosheets. *Angew. Chem. Int. Ed.* **2009**, *48*, 6861–6864.

39. Pang, Y.; Uddin, M. N.; Chen, W.; Javaid, S.; Barker, E.; Li, Y.; Suvorova, A.; Saunders, M.; Yin, Z.; Jia, G. Colloidal Single-Layer Photocatalysts for Methanol-Storable Solar H_2 Fuel. *Adv. Mater.* **2019**, *31*, 1905540.

40. Wang, A.; Hu, X.; Wang, F.; Chen, W.; Pang, Y.; Javaid, S.; Chen, D.; Li, X.; Staaden, L.; Jia, G. Large Lateral Sized Two-Dimensional $Cu_{2-x}S$ Nanoplates Formed by Ostwald Ripening. *Mater. Lett.* **2019**, *237*, 88–91.

41. Luther, J. M.; Jain, P. K.; Ewers, T.; Alivisatos, A. P. Localized Surface Plasmon Resonances Arising From Free Carriers in Doped Quantum Dots. *Nat. Mater.* **2011**, *10*, 361–366.

42. Elimelech, O.; Liu, J.; Plonka, A. M.; Frenkel, A. I.; Banin, U. Size Dependence of Doping by a Vacancy Formation Reaction in Copper Sulfide Nanocrystals. *Angew. Chem. Int. Ed.* **2017** *56*, 10335–10340.

43. Jen-La Plante, I.; Teitelboim, A.; Pinkas, I.; Oron, D.; Mokari, T. Exciton Quenching Due to Copper Diffusion Limits the Photocatalytic Activity of CdS/Cu_2S Nanorod Heterostructures. *J. Phys. Chem. Lett.* **2014**, *5*, 590–596.

44. Chen, D.; Wang, A.; Buntine, M. A.; Jia, G. Recent Advances in Zinc-Containing Colloidal Semiconductor Nanocrystals for Optoelectronic and Energy Conversion Applications. *ChemElectroChem* **2019**, *6*, 4709–4718.

45. Mora-Fonz, D.; Lazauskas, T.; Farrow, M. R.; Catlow, C. R. A.; Woodley, S. M.; Sokol, A. A. Why Are Polar Surfaces of ZnO Stable? *Chem. Mater.* **2017**, *29*, 5306–5320.

46. Kresse, G.; Dulub, O.; Diebold, U. Competing Stabilization Mechanism for the Polar ZnO(0001)-Zn Surface. *Phys. Rev. B* **2003**, *68*, 245409.

47. Lauritsen, J. V.; Porsgaard, S.; Rasmussen, M. K.; Jensen, M. C. R.; Bechstein, R.; Meinander, K.; Clausen, B. S.; Helveg, S.; Wahl, R.; Kresse, G.; Besenbacher, F. Stabilization Principles for Polar Surfaces of ZnO. *ACS Nano* **2011**, *5*, 5987–5994.

48. Li, J.; Gayles, J.; Kioussis, N.; Zhang, Z.; Grein, C.; Aqariden, F. Ab Initio Studies of the Unreconstructed Polar CdTe (111) Surface. *J. Electron. Mater.* **2012**, *41*, 2745–2753.

49. Kresse, G.; Joubert, D. From Ultrasoft Pseudopotentials to the Projector Augmented-Wave Method. *Phys. Rev. B* **1999**, *59*, 1758–1775.

50. Blöchl, P. E. Projector Augmented-Wave Method. *Phys. Rev. B* **1994**, *50*, 17953–17979.